Strain-Driven Oxygen Deficiency in Self-Assembled, Nanostructured, Composite Oxide Films

Claudia Cantoni,[†,*] Yanfei Gao,[‡,§] Sung Hun Wee,[†] Eliot D. Specht,[†] Jaume Gazquez,[†] Jianyong Meng,[§] Stephen J. Pennycook,[†] and Amit Goyal[†]

[†]Materials Science and Technology Division, Oak Ridge National Laboratory, Oak Ridge, Tennessee 37831-6116, Unites States, [‡]Computer Science and Mathematics Division, Oak Ridge National Laboratory, Oak Ridge, Tennessee 37831-6164, United States, and [§]Department of Materials Science and Engineering, University of Tennessee, Knoxville, Tennessee 37996-2200, United States.

Within the field of metal oxides, nanocomposite films with novel functionality have been recently synthesized by spontaneous assembly of nanodots or nanorods of one material embedded in the matrix of another material.[1−7] This approach has been successfully employed to fabricate multiferroics and magnetoelectric nanocomposites by coupling ferroelectric and magnetostrictive components for application in spintronics, information storage, and logic devices.[1−3] Other successful applications include thermoelectric composites[4] and high-T_c superconductors, in which enhanced performance is obtained by self-assembly of nonsuperconducting oxide nanorods within the superconductor matrix.[5,6] The latter nanocomposite system is of general interest as a model for other oxide-based nanocomposites in which enhanced or novel functionality arises from strain coupling of the constituent phases. As oxide-based nanocomposites form a new and very incomplete area of research, little is known about the relationships between functionality, nanocomposite microstructure, and strain and composition modulations at the nanoscale. Nanocomposites incorporating superconductors can be useful in advancing our fundamental understanding of functional oxide nanocomposites in general because of the wealth of existing knowledge about superconductive properties and the way they change with the addition of nanosized correlated defects and second phases. For example, flux pinning and critical current are well-known to be extremely sensitive not only to shape, order, and size of embedded nanoparticles but also to more subtle changes in interfacial composition and lattice defects on a subnanometer scale.

ABSTRACT Oxide self-assembly is a promising bottom-up approach for fabricating new composite materials at the nanometer length scale. Tailoring the properties of such systems for a wide range of electronic applications depends on the fundamental understanding of the interfaces between the constituent phases. We show that the nanoscale strain modulation in self-assembled systems made of high-T_c superconducting films containing nanocolumns of BaZrO$_3$ strongly affects the oxygen composition of the superconductor. Our findings explain the observed reduction of the superconducting critical temperature.

KEYWORDS: self-assembly · thin-film nanocomposites · nanorods · strain · superconductors · scanning transmission electron microscopy

Here we present a detailed investigation of interfacial structure and chemistry in composite films made of BaZrO$_3$ (BZO) self-assembled nanocolumns within a RE-Ba$_2$Cu$_3$O$_{7-\delta}$ (REBCO; RE: rare earth, Y, or mixture of Y and rare earth) high-T_c superconductive matrix. We combine finite element and analytical strain field calculations, X-ray diffraction (XRD), and atomic resolution Z-contrast scanning transmission electron microscopy (Z-STEM) coupled with electron energy loss spectroscopy (EELS) to show that the local strain induces oxygen deficiency in the superconductive matrix, which leads to a significant reduction in the long-range superconducting properties. The region of degraded superconductivity extends for several nanometers around each nanocolumn, implying that a maximum useful density exists for optimized properties. On the basis of these findings, we propose impurity doping as a mean to relieve strain and suppress formation of O vacancies, thereby improving superconductivity around the nanocolumns.

The mechanism responsible for solid-state self-assembly is largely related to the strain field that develops around the nanoscale second phases embedded in the

matrix and to the reduction of phase boundary energy. Theoretical formulations based on energetic and kinetic arguments (which will be discussed in detail in a future publication) specify an optimal range of 4−12% for the lattice mismatch of the embedded phase with respect to the REBCO matrix. The resulting nanocolumns extend for nearly the entire film thickness and consist of long, continuous nanorods or stacks of shorter nanorods.

The ordered array of BZO nanocolumns in REBCO was obtained by simultaneous deposition of REBCO and BZO either by performing laser ablation from a BZO-doped YBCO target or by adding Zr to the liquid precursor in a metal organic chemical vapor deposition (MOCVD) reactor. Details of film deposition are reported elsewhere.[8,9] All composite films were grown epitaxially on biaxially textured, buffered hastelloy tapes.[10] STEM and EELS data were acquired in a dedicated STEM, VG Microscopes HB501UX, operated at 100 kV and equipped with an Enfina EEL spectrometer and a Nion aberration corrector.

Figure 1A shows the microstructure of a 0.8 μm thick, 4 vol % BZO-doped YBCO film made *via* pulsed laser deposition (PLD). A mismatch of ∼8% is found between three BZO perovskite unit cells (a = 4.193 Å) and the tripled perovskite blocks that make up the YBCO cell. The mismatch occurs along the vertical interfaces between the nanocolumns and the matrix with the epitaxial relationship BZO(001)//YBCO(001)//surface normal; BZO(100)//YBCO(100). The out-of-plane strain distribution that arises from this misfit can be calculated by a finite element method and is shown in Figure 1B,C for two values of the ratio between nanocolumn length, d, and distance between nanocolumns, L, representing the cases of a dilute and concentrated distribution of BZO nanocolumns in the host matrix, respectively. The films considered here fall in the concentrated limit of Figure 1C. When panels B and C of Figure 1 are compared, it is evident that an increased concentration of BZO nanocolumns leads to a larger overall positive strain of the REBCO along the c axis, resulting in an average increase of the c lattice parameter. In real systems, misfit dislocations form at the interfaces around precipitates and affect the local strain field together with inhomogeneities in cation or oxygen composition. The microstrain in each composite film can be measured *via* XRD by analyzing the width of multiple REBCO Bragg peaks displayed in a Williamson−Hall plot.[11] As expected, the microstrain also increases with increasing BZO concentration, as shown in Figure 1D, where a comparison is made between simulated strain and strain extracted by XRD as a function of BZO volume fraction. As the plot shows, the experimental slope is reduced to nearly 24% of the simulation for the case d/L = 20 and coherent interface, indicating that 76% of the original misfit has been relieved and the effective residual

misfit strain is ∼24% × 8% = 1.9%. This reduction is caused by misfit dislocations that form at the YBCO/BZO interface, giving rise to a semicoherent REBCO/BZO phase boundary. Figure 1D also shows the strain calculated by finite element simulation in the presence of misfit dislocations at the BZO/YBCO phase boundary for the less computationally intensive case of d/L = 1. These values are much closer to the experimental data, further supporting the presence of interface dislocations in the system. The incoherent phase boundary is modeled by solving the lattice disregistry field and thus determining the defect density from the balance of the disregistry-induced interplanar energy and the long-range elastic interaction.[12]

In addition to an increase in strain, a nearly linear reduction of T_c is observed with increasing BZO concentration that amounts to roughly 0.4 K for unitary change in BZO concentration expressed in vol %. Figure 2 shows the superconducting critical temperature obtained through four-probe resistive measurements for PLD and MOCVD films as a function of the BZO concentration measured by XRD. Both PLD and MOCVD films show a similar decrease in T_c with increasing BZO concentration as better visualized by the plot of ΔT_c shown in Figure 2B. We note that variations as large as 0.5 K are typically observed for the T_c of nominally identical REBCO films. Therefore, the present data do not provide a definitive answer for the behavior of T_c at small BZO concentrations up to ∼4 vol %. However, above this concentration, the decrease in T_c is clearly larger than any sample-to-sample variation.

For atomic scale information on structure and composition, we use aberration-corrected Z-STEM coupled with EELS. The BZO nanocolumns have a width of 6−8 nm, while our typical TEM foils, prepared by the focused ion beam technique, have a thickness of about 30−40 nm. Consequently, in most TEM samples, the BZO nanocolumns are covered by several REBCO atomic planes, and this superimposition results in moiré fringes rather than clear BZO lattice fringes (see Figure 1A). In the case of Figure 3, a single BZO rod has been sectioned by the TEM preparation process along most of its entire length, offering the opportunity to view the details of its interface with the REBCO lattice. For this particular MOCVD film, the BZO volume fraction, as measured by X-rays, is 4.1% and RE is a mixture of Y and Gd. Figure 3B is a high-resolution Z-STEM micrograph of the nanocolumn in Figure 3A and clearly shows that the BZO c axis and the REBCO c axis are tilted with respect to each other by nearly 3°. This commonly observed tilt is accommodated by introduction of dislocations, some of which are pure tilt dislocations with Burgers vector 1/2(100), as indicated by circles. The images also reveal misfit dislocations with Burgers vector 1/2(101), which are active in relieving misfit strain (arrows in Figure 3B). The
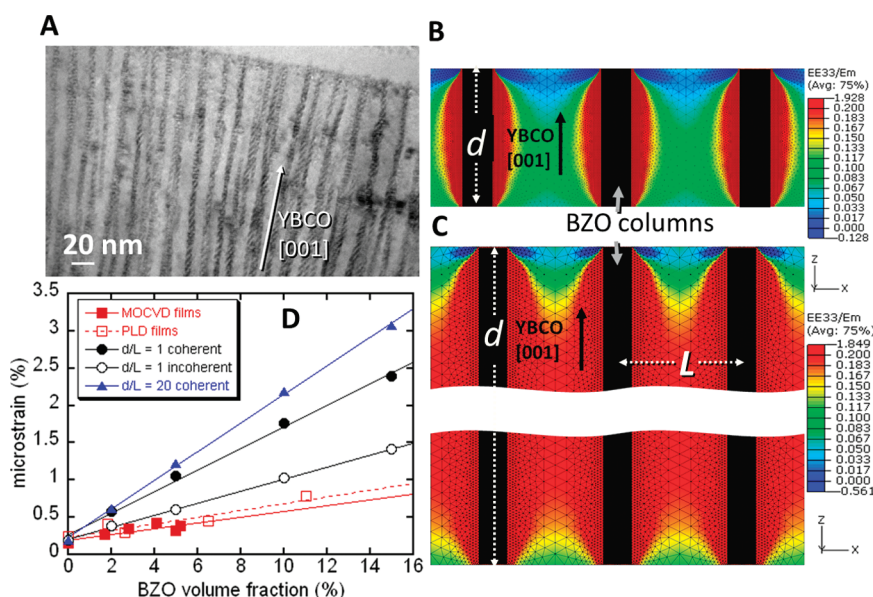
Figure 1. Evaluation of strain in BZO-doped REBCO composite films. (A) TEM micrograph illustrating the morphology of a 4 vol % BZO nanocolumn array embedded in the YBCO matrix. (B,C) Volumetric average of the out-of-plane strain (ε_{33}/f_o; f_o= lattice misfit) calculated through finite element method for the cases $d/L = 1$ (B) and $d/L = 20$ (C). (D) Strain *versus* BZO concentration as calculated by the finite element method for the cases $d/L = 20$ coherent interface (blue triangles), $d/L = 1$ coherent interface (black dots), $d/L = 1$ incoherent interface (black circles), and measured by X-ray diffraction for PLD films (red, open squares) and MOCVD films (red, filled squares).
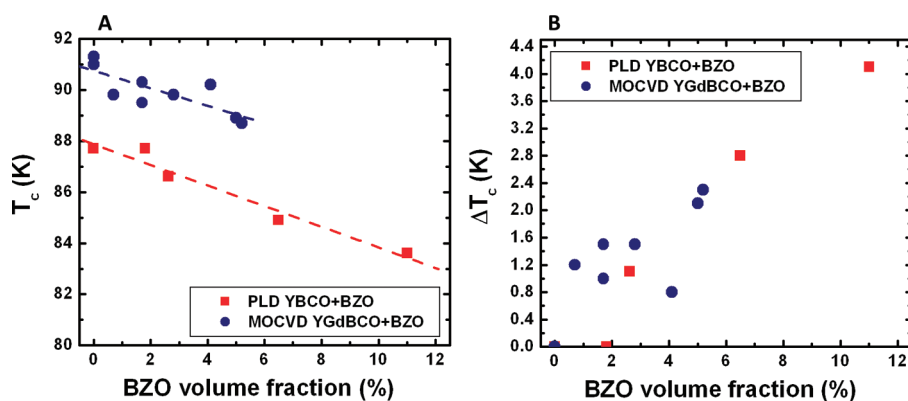

Figure 2. Critical temperature (T_c) obtained by resistivity *vs* temperature measurements for PLD and MOCVD BZO-doped REBCO films. (A) T_c dependence on BZO concentration. (B) Plot of variations of T_c (ΔT_c) with respect to the T_c of undoped REBCO samples.

average spacing between these dislocations is ~3 YBCO unit cells (3.5 nm). A similar average spacing $\bar{D}$ can be calculated using the equation $\bar{D} = b_z/(f_o - \varepsilon_o)$, where f_o defines the original misfit between lattices, ε_o is the residual misfit strain, and b_z is the Burgers vector component along the interface plane. Choosing $\varepsilon_o = 1.9\%$ as calculated above, gives $\bar{D} = 2.7$ YBCO unit cells, showing excellent agreement between STEM and XRD results. The REBCO lattice surrounding the BZO nanorod shows a brighter contrast than the REBCO well within the matrix. The same region gives an even larger (and inverted) contrast in the bright field (BF) image acquired simultaneously to Figure 3B (see Figure 3C), strongly suggesting the presence of significant strain localized in the REBCO lattice surrounding the BZO nanocolumn.

The local strain can be quantified directly through the Z-STEM images by measuring the variation of the REBCO c axis parameter. Figure 3D shows the result of such a measurement where the c axis spacing is obtained by fitting Gaussian curves to the intensity of the Ba and Y/Gd columns in the dashed box of Figure 3B. About 13 values for c were calculated at each basal unit cell increment along the x direction and the average $\bar{c}$ plotted in Figure 3D as ($\bar{c} - c_o)/c_o$, where c_o is the c parameter well within the matrix. The measured strain increases when moving from the matrix interior toward the BZO nanorod until it reaches a maximum at a distance of ~5 nm from the interface. Then, in close proximity to the BZO interface, the strain decreases rapidly over a distance of about 3 nm. The end part of the plot, around $x = -2$ nm, corresponds to

ARTICLE
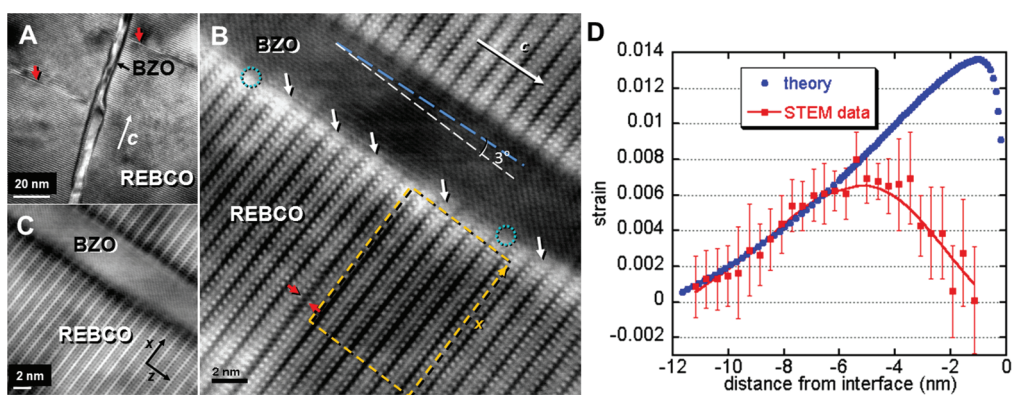
Figure 3. Local lattice deformation by high-resolution STEM imaging. (A) TEM micrograph of a sectioned BZO nanocolumn. (B) High-resolution Z-STEM image of the same nanocolumn in A. Dashed blue and white lines indicate the direction of the *c* axes of BZO and REBCO, respectively, showing a 3° tilt between the two lattices. Light blue circles indicate pure tilt dislocations; white arrows indicate misfit dislocations. (C) BF image acquired simultaneously to image B. (D) Comparison between analytically calculated strain (blue dots) and experimentally derived strain (red squares). The experimental strain is expressed using a *c* parameter obtained from interatomic distances within the yellow box in B. Red arrows in A and B indicate intergrowths having the Y124 structure.

the beginning of the region where dislocations and strong contrast are observed in the images. In this narrow REBCO strip, the tilt and misfit dislocations cause strong lattice distortions. These distortions are associated with high local strains that can have both compressive and tensile components which cause small atomic displacements along the columns. Such displacements give rise to strain contrast for moderate detector angles as used here, explaining the bright band seen in the Z-contrast image from this region.[13,14] The local strain distribution near the REBCO/BZO boundary was also predicted by analytically solving the anisotropic elastic boundary value problem of the bimaterial interface dislocations.[15] The analytic result is plotted against the experimental data in Figure 3D. The theoretical trend is similar to the data extracted by Z-STEM with some difference in the location and magnitude of the peak. Although the finite dimension of the BZO column, which is not accounted for by the model, plays a small role, oxygen deficiency near the interface, which we discuss below, provides an important strain relieving mechanism in addition to the interface dislocations. The microstrain observed by Z-STEM for this sample is 0.6 ± 0.3%. If we compare this value with 0.42%, the experimental microstrain obtained by XRD and shown in Figure 1D, we find a good agreement between direct Z-STEM measurements and XRD analysis.

The relationship between transition temperature and epitaxial strain in REBCO is complicated by the anisotropic crystal structure, which leads to transport properties that are different for each of the principal crystal axes. Studies on untwinned YBCO single crystals have shown that the pressure derivatives $dT_c/dp_{a,b}$ are large and opposite in sign for compression in the *ab* plane, with $dT_c/dp_a = -2.0 \pm 0.2$ K/GPa and $dT_c/dp_b = 1.9 \pm 0.2$ K/GPa. The pressure derivative for *c* axis

compression is smaller and negative, $dT_c/dp_c = -0.3 \pm 0.1$ K/GPa for fully oxygenated YBCO.[16] Considering that the dominant effects, which occur along *a* and *b*, are similar in magnitude and opposite in sign, and that the REBCO films are generally twinned in the *ab* plane with equal population of twin domains, we would not expect significant T_c suppression on the sole basis of strain arguments.

To investigate additional causes of T_c suppression, we conducted a chemical analysis of the YBCO/BZO interfaces using EELS. Figure 4A shows the results of an EELS line scan conducted across the nanocolumn in Figure 3. For clarity, only the Y-$M_{4,5}$, Ba-$M_{4,5}$, and O-K integrated intensities are plotted. We notice that while the Y signal is greatly reduced, the Ba and O signals are enhanced within the nanocolumns, as expected based on the observation that BZO contains more Ba and O atoms per unit volume than YBCO. Overall, the interface between BZO and REBCO is well-defined, and the EELS scan does not suggest any reaction or major intermixing between the two phases, in agreement with the known stability and inertness toward REBCO reported for BZO.[17] In addition, we observe an interesting behavior for the O signal. The O profile shows a depression in the YBCO region immediately adjacent to the BZO column (see arrows in Figure 4) before it reaches a value characteristic of the matrix oxygen content. Such behavior is not observed in the Ba signal, which exhibits a nearly constant value immediately past the interface. Y and Gd signals are more intricate because of the presence of (Y,Gd)$_2$O$_3$ nanoparticles in these films. To analyze this effect in more detail and reject the possibility of an artifact in the line scans, EELS maps were also acquired in various regions. One of these maps is shown in Figure 4B. Each map pixel relates to a different EELS spectrum, and for each pixel, the annular dark field (ADF) signal was acquired

CANTONI *ET AL.*

VOL. 5 ▪ NO. 6 ▪ 4783–4789 ▪ 2011

ACSNANO

4786

www.acsnano.org
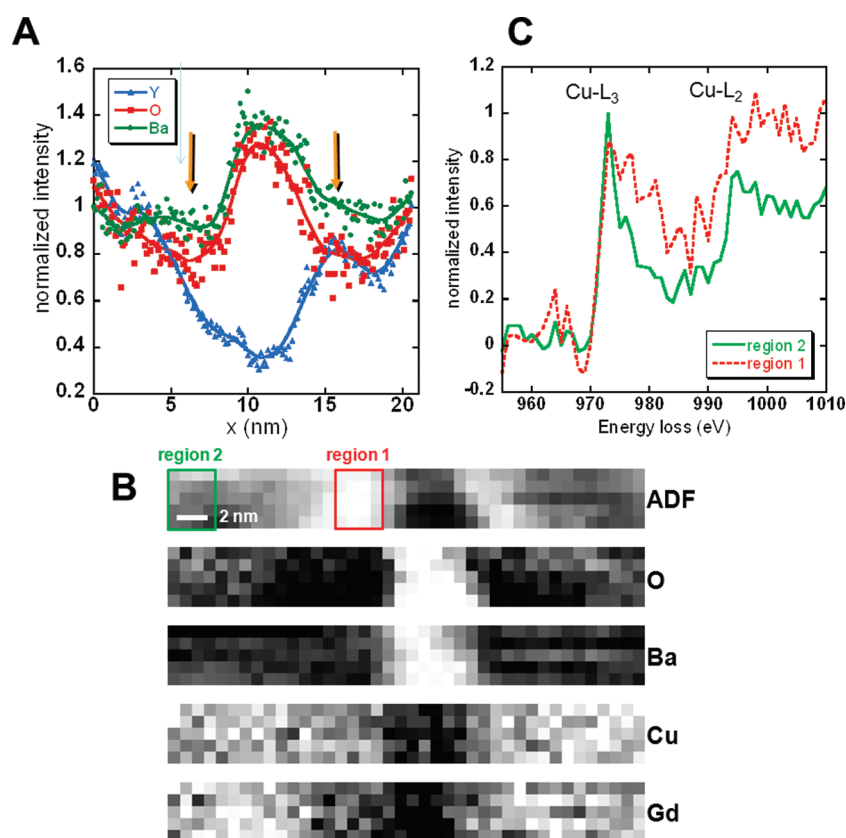
Figure 4. Results of EELS analysis. (A) Integrated intensity profiles of Y-$M_{4,5}$, O-K, and Ba-$M_{4,5}$ across the BZO nanocolumn of Figure 3. **(B)** EELS maps of O-K, Ba-$M_{4,5}$, Cu-$L_{2,3}$, and Gd-$M_{4,5}$. The top map is the signal from the ADF detector acquired simultaneously to each spectrum. The yellow arrows highlight the suppressed O signal in proximity of the nanocolumn. **(C)** Comparison of Cu-$L_{2,3}$ edges after removal of plural scattering by deconvolution for the regions labeled 1 and 2 in B.

simultaneously with the EELS data, as shown in the top image of Figure 4B. Analogously to Figure 3B, the ADF signal shows a large intensity (bright contrast) in the REBCO region immediately adjacent to the BZO rod. The region showing the brightest shade in the ADF map appears as darkest in the O-K map (see second image from top in Figure 4B). The O signal shows a maximum value in the interior of the BZO rod, a minimum value in the YBCO region immediately sur-rounding the rod, and an intermediate value further away from the BZO rod. In contrast, the Ba and Cu maps show maximum and minimum values, respectively, within the BZO rod and exhibit a constant contrast level everywhere else in the surrounding REBCO ma-trix. Since the ADF signal is not sensitive to light species such as O and the heavier atoms show a constant concentration outside the BZO rod, the bright contrast in the ADF map should be related to strain. The dark contrast in the O map cannot be determined by dechanneling and high-angle scattering of a portion of the incident electron beam, which is therefore not collected by the EELS detector. If this were the case, a similar dark contrast would be observed in the cation maps as well. These observations not only confirm the line scan findings but also suggest, through the corre-lation between ADF and O signals, that the strain in the

REBCO lattice surrounding the BZO rod and the oxygen deficiency are correlated. As an alternative method to detect oxygen deficiency, we probed the Cu valence state by analyzing the Cu-$L_{2,3}$ edge well inside the REBCO matrix and in the region adjacent to the BZO rod.[18] Figure 4C shows this analysis performed for two different regions in the spectrum image in Figure 4B. As shown by the ratio of the L_3 and L_2 lines, the Cu valence is lower in region 1, adjacent to the BZO rod than in region 2, within the REBCO matrix. The same behavior for the Cu-$L_{2,3}$ edges is observed in all of the spectrum images acquired and independently on the number of pixels chosen for regions 1 and 2, indicating that the oxygen deficiency is present everywhere within the strained region surround-ing the nanorods and is not localized in certain points.

It is important to point out that depletion of oxygen in the REBCO phase by the more thermodynamically stable BZO phase is unlikely because all of the REBCO films analyzed here were grown at an oxygen pressure well above the equilibrium pressure for REBCO stabi-lity. In addition, BZO-free REBCO films grown in the same conditions as the films analyzed here did not show any evidence of oxygen deficiency. The oxygen deficiency observed here is likely the consequence of the high strain experienced by the YBCO lattice in the dislocation-decorated region at the BZO interface,

similarly to what has been reported for YBCO grain boundaries.[19] Within this picture, the strain would hinder proper REBCO oxygenation, and this substoichiometry would, in turn, lower the strain near the phase boundary, partially explaining the discrepancy with analytical calculations (Figure 3D). The existence of a relationship between film stress and oxygen nonstoichiometry has already been reported by others.[20,21]

The overall conclusion from the O maps and line scans is that the oxygen-deficient REBCO stretches over a region of outer diameter equal to 3−4 times the BZO rod diameter. It is known that oxygen deficiency readily suppresses T_c in REBCO.[22] Considering that the diameter of the BZO rods are 6−8 nm and the average spacing between BZO rods is ∼20 nm for a BZO concentration of 4 vol %, an overlap of oxygen-depleted REBCO regions surrounding BZO nanocolumns is expected to occur near or above this concentration,

leading to the disruption of current percolation through the high T_c phase and, consequently, to a lower measured T_c. Disruption of current percolation above a certain BZO concentration is likely to occur in our self-assembled BZO−REBCO systems, in which the BZO rods are distributed with a high degree of order within the REBCO matrix.[23]

We have shown direct evidence of microstrain and its resulting effect on anion composition. The strain is localized around the BZO nanocolumns over distances of a few nanometers. EELS spectrum imaging shows oxygen deficiency within the strained regions of REBCO. On the basis of an analogy with the oxygen depletion at strained REBCO grain boundaries and its mitigation by introduction of impurity species (e.g., Ca),[19,24] this work suggests that doping might be effective in locally raising T_c and hence the superconducting properties of these composite films.

METHODS

Film Deposition. The ordered array of BZO nanocolumns in REBCO was obtained by simultaneous deposition of REBCO and BZO either by performing laser ablation from a BZO-doped YBCO target[8] or by adding Zr to the liquid precursor in an MOCVD reactor.[9] In the PLD process, the BZO-doped YBCO target was obtained using BZO nanoparticles commercially available with a particle size distribution ranging from 10 to 100 nm. The nanoparticles were mixed with YBCO powder, and the resulting composite powder was pressed and sintered at 950 °C for 2 h. The PLD growth temperature was 790 °C, and the oxygen partial pressure was 230 mTorr. In the MOCVD process, tetramethyl heptanedionate (thd) precursors were vaporized from a solution and the vapors were injected over the deposition area in a carrier gas of Ar.[25] Substrate temperature of 800 to 850 °C and reactor pressure of 2 to 3 Torr were used. Zr was added in form of $Zr(thd)_4$ to the rest of the precursors in amounts ranging from 5 to 10 atom %. All composite films were grown epitaxially on buffered hastelloy tapes in which a sharp cubic biaxial texture was obtained by ion beam assisted deposition (IBAD) of MgO followed by homoepitaxial MgO and an epitaxial $LaMnO_3$ cap layer.[10] The MOCVD films and the substrates were provided by SuperPower Inc. Film thickness ranged between 0.4 and 0.8 μm, column diameter was ∼6−8 nm, and average nanocolumn separation ranged from ∼50 nm for 1% BZO doping to ∼15 nm for 10% doping.

Atomic Resolution Z-Contrast Imaging and EELS. STEM and EELS data were acquired in a dedicated STEM, VG Microscopes HB501UX, operated at 100 kV and equipped with an Enfina EEL spectrometer and a Nion aberration corrector. In this microscope, the aberration-corrected probe yields a routine spatial resolution of 1.1 Å, and the high-angle annular dark field detector allows recording incoherent Z-contrast images, in which the contrast of an atomic column is approximately proportional to the square of the average atomic number (Z). In this situation, the brightest spots in Figure 3B represent the heavy Ba columns, while the lighter Cu−O columns appear dark, with the darkest contrast shown by the atomic planes containing Cu−O chains. The annular detector geometry makes it possible to collect the electons scattered at large angles and, simultaneously, those traveling closer to the optical axis through the dark field detector hole, which form a bright field (BF) image, giving complementary information as shown in Figure 3. The EELS spectra were acquired with an energy

dispersion of 1 eV in order to simultaneously record the Y-M, O-K, Ba-M, Cu-L, and Gd-M edges. Spectra were acquired with a dwell times ranging between 0.5 and 1.8 s. Sample drift and damage were checked after each acquisition. The spectra were then background subtracted and the signal of each edge was integrated. TEM foils were prepared by the focus ion beam (FIB) technique, followed by low voltage ion milling and plasma cleaning.

X-ray Analysis Method. X-ray diffraction patterns were measured in Bragg−Brentano geometry using a Cu source operating at 50 kV and 100 mA and a Peltier-cooled energy-dispersive Si(Li) detector tuned to Cu Kα. Samples were tilted for alignment with the YBCO(00L) reflections. Peak widths were determined by least-squares fitting to a skewed Lorentzian: $I_L(2\theta) = I_L^1(2\theta) + I_L^1(2\theta + \delta)$, where $\delta = 0.00496 \tan(\theta)$ is the $K\alpha_1/K\alpha_2$ splitting and

$$I_L^1(2\theta) = \frac{A_L}{(2\theta - 2\theta_L)^2 + \kappa_L^2} + B_L$$

with $\kappa = \kappa_L^+$ for $2\theta > 2\theta_L$ and $\kappa = \kappa_L^-$ for $2\theta < 2\theta_L$. Angles are in radians. Free parameters are A_L, B_L, $2\theta_L$, κ_L^+, and $\kappa = \kappa_L^-$. Peaks were fitted for $L = 1-11$, omitting the weak (008) reflection. Lattice parameter c was determined by least-squares fitting to

$$L\lambda = 2c \sin(\theta_L + D \cos\theta_L)$$

with $\lambda = 0.154056$ nm. Free parameters are c and D, which corrects for sample displacement. Resolution-corrected peak FWHM is given by $\Delta 2\theta_L = [(\kappa_L^+ + \kappa_L^-)^2 + 0.0012^2]^{1/2}$. The last term is the FWHM of a LaB_6 powder used to determine instrumental broadening. Microstrain $\Delta d/d$ was found by least-squares fitting to the Williamson−Hall line:

$$\Delta 2\theta \cos\theta = \frac{0.9\lambda}{T} + 2\frac{\Delta d}{d} \sin\theta$$

Free parameters are $\Delta d/d$ and T, which is a measure of particle size.

Theoretical Calculations. A three-dimensional finite element method was used to compute the strain development in the matrix. The lattice-mismatch-induced stress fields are equivalent to applying tractions on the BZO phase boundaries. Reported strains in Figure 1D are averaged over the entire matrix. The incoherent phase boundary is modeled by solving the lattice disregistry field from the balance of the disregistry-induced

interplanar energy and the long-range elastic interaction.[12] The theoretical interface strength is chosen to be 1/50 of the c_{11} modulus of YBCO. Dislocations nucleate on the interface as a result of large lattice mismatch. The strain field near the YBCO/BZO boundary in Figure 3D is calculated analytically by solving the elasticity boundary value problem of interface dislocations lying on a bimaterial interface. The solution method combines the Stroh formalism for anisotropic elasticity and analytic continuation technique.[15] Locations of misfit and tilt dislocations are based on Z-STEM image in Figure 3B.

REFERENCES AND NOTES

1. Zheng, H.; Wang, J.; Lofland, S. E.; Ma, Z.; Mohaddes-Ardabili, L.; Zhao, T.; Salamanca-Riba, L.; Shinde, S. R.; Ogale, S. B.; Bai, F.; *et al.* Multiferroic BaTiO₃-CoFe₂O₄ Nanostructures. *Science* **2004**, *303*, 661–663.

2. Zavaliche, F.; Zheng, H.; Mohaddes-Ardabili, L.; Yang, S. Y.; Zhan, Q.; Shafer, P.; Reilly, E.; Chopdekar, R.; Jia, Y.; Wright, P.; *et al.* Electric Field-Induced Magnetization Switching in Epitaxial Columnar Nanostructures. *Nano Lett.* **2005**, *5*, 1793–1796.

3. Eerenstein, W.; Mathur, N. D.; Scott, J. F. Multiferroic and Magnetoelectric Materials. *Nature* **2006**, *442*, 759–765.

4. Kosuga, A.; Kurosaki, K.; Yubuta, K.; Charoenphakdee, A.; Yamanaka, S.; Funahashi, R. Solid-State Self-Assembly of Nanostructured Oxide as a Candidate High-Performance Thermoelectric Material. *J. Electron. Mater.* **2009**, *38*, 1303–1308.

5. Kang, S.; Goyal, A.; Li, J.; Gapud, A. A.; Martin, P. M.; Heatherly, L.; Thompson, J. R.; Christen, D. K.; List, F. A.; Paranthaman, M.; *et al.* High-Performance High-T_c Superconducting Wires. *Science* **2006**, *311*, 1911–1914.

6. Wee, S. H.; Goyal, A.; Li, J.; Zuev, Y. L.; Cook, S. Strong Enhancement of Flux Pinning in Thick NdBa₂Cu₃O₇₋δ Films Grown on Ion-Beam Assisted Deposition-MgO Templates *via* Three-Dimensional Self-Assembled Stacks of BaZrO₃ Nanodots. *J. Appl. Phys.* **2007**, *102*, 063906–063911.

7. Yang, H.; Wang, H.; Yoon, J.; Wang, Y.; Jain, M.; Feldmann, D. M.; Dowden, P. C.; MacManus-Driscoll, J. L.; Jia, Q. Vertical Interface Effect on the Physical Properties of Self-Assembled Nanocomposite Epitaxial Films. *Adv. Mater.* **2009**, *21*, 3794–3798.

8. Wee, S. H.; Goyal, A.; Zuev, Y. L.; Cantoni, C. High Performance Superconducting Wire in High Applied Magnetic Fields *via* Nanoscale Defect Engineering. *Supercond. Sci. Technol.* **2008**, *21*, 092001–092004.

9. Chen, Y.; Selvamanickam, V.; Zhang, Y.; Zuev, Y. L.; Cantoni, C.; Specht, E. D.; Paranthaman, M.; Aytug, T.; Goyal, A.; Lee, D. F. Enhanced Flux Pinning by BaZrO₃ and (Gd,Y)₂O₃ Nanostructures in Metal Organic Chemical Vapor Deposited GdYBCO High Temperature Superconductor Tapes. *Appl. Phys. Lett.* **2009**, *94*, 062513–062515.

10. Xiong, X.; Lenseth, K. P.; Reeves, J. L.; Rar, A.; Qiao, Y.; Schmidt, R. M.; Chen, Y.; Li, Y.; Xie, Y.; Selvamanickam, V. High Throughput Processing of Long-Length IBAD MGO and Epi-Buffer Templates at Superpower. *IEEE Trans. Appl. Supercond.* **2007**, *17*, 3375–3378.

11. Cullity, B. D.; Stock, S. R. *Elements of X-ray Diffraction*, 3rd ed.; Prentice Hall: Upper Saddle River, NJ, 2001; Chapter 3.

12. Rice, J. R. Dislocation Nucleation from a Crack Tip: An Analysis Based on the Peierls Concept. *J. Mech. Phys. Solids* **1992**, *40*, 239–271.

13. Duscher, G.; Pennycook, S. J.; Browning, N. D.; Rupangudi, R.; Takoudis, C.; Gao, H. J.; Singh, R. In *Characterization and Metrology for ULSI Technology*; Seiler, D. G., Diebold, A. C., Bullis, W. M., Shaffner, T. J., Mcdonald, R., Walters, E. J., Eds.; AIP: New York, 1998; Vol. 449, pp 191–195.

14. Yu, Z. H.; Muller, D. A.; Silcox, J. Study of Strain Fields at a-Si/c-Si Interface. *J. Appl. Phys.* **2004**, *95*, 3362–3371.

15. Yu, H. H.; Shrotriya, P.; Gao, Y. F.; Kim, K.-S. Micro-Plasticity of Surface Steps under Adhesive Contact: Part I—Surface Yielding Controlled by Single-Dislocation Nucleation. *J. Mech. Phys. Solids* **2007**, *55*, 489–516.

16. Welp, U.; Grimsditch, M.; Fleshler, S.; Nessler, W.; Downey, J.; Crabtree, G. W. Effect of Uniaxial Stress on the Superconducting Transition in YBa₂Cu₃O₇. *Phys. Rev. Lett.* **1992**, *69*, 2130–2133.

17. Palouse, K. V.; Koshy, J.; Damodaran, A. D. Superconductivity in YBa₂Cu₃O₇-ZrO₂ Systems. *Supercond. Sci. Technol.* **1991**, *4*, 98–101.

18. Grioni, M.; van Acker, J. F.; Czyžyk, M. T.; Fuggle, J. C. Unoccupied Electronic Structure and Core-Hole Effects in the X-ray-Absorption Spectra of Cu₂O. *Phys. Rev. B* **1992**, *45*, 3309–3318.

19. Klie, R. F.; Buban, J. P.; Varela, M.; Franceschetti, A.; Jooss, C.; Zhu, Y.; Browning, N. D.; Pantelides, S. T.; Pennycook, S. J. Enhanced Current Transport at Grain Boundaries in High-T_c Superconductors. *Nature* **2005**, *435*, 475–478.

20. Bozovic, I.; Logvenov, G.; Belca, I.; Narimbetov, B.; Sveklo, I. Epitaxial Strain and Superconductivity in La₂₋ₓSrₓCuO₄ Thin Films. *Phys. Rev. Lett.* **2002**, *89*, 107001(4).

21. Klenov, D. O.; Donner, W.; Foran, B.; Stemmer, S. Impact of Stress on Oxygen Vacancy Ordering in Epitaxial (La₀.₅Sr₀.₅)CoO₃₋δ Thin Films. *Appl. Phys. Lett.* **2003**, *82*, 3427–3429.

22. Jorgensen, J. D.; Veal, B. W.; Paulikas, A. P.; Nowicki, L. J.; Crabtree, G. W.; Claus, H.; Kwok, W. K. Structural Properties of Oxygen-Deficient YBa₂Cu₃O₇. *Phys. Rev. B.* **1990**, *41*, 1863–1877.

23. Cantoni, C.; Goyal, A. Nanomaterials for Superconductors from the Energy Perspective. In *Nanotechnology for the Energy Challenge*; Garcia-Martinez, J., Ed.; Wiley-VCH Verlag GmbH & Co. KGaA: Weinheim, Germany, 2010; Chapter 9.

24. Hammerl, G.; Schmehl, A.; Schulz, R. R.; Goetz, B.; Bielefeldt, H.; Schneider, C. W.; Hilgenkamp, H.; Mannhart, J. Enhanced Supercurrent Density in Polycrystalline YBa₂Cu₃O₇₋δ at 77 K from Calcium Doping of Grain Boundaries. *Nature* **2000**, *407*, 162–164.

25. Selvamanickam, V.; Xie, Y.; Reeves, J. L.; Chen, Y. MOCVD-Based YBCO-Coated Conductors. *MRS Bull.* **2004**, *29*, 579–582.